Ocean Engineering 287 (2023) 115745

Contents lists available at ScienceDirect

Ocean Engineering

journal homepage: www.elsevier.com/locate/oceaneng

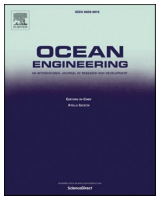

Feasibility study on mimicking the tail-beating supported gliding flight of flying fish

Khanh Nguyen, Hoon Cheol Park *

Department of Smart Vehicle Engineering, Artificial Muscle Research Center, Konkuk University, Seoul, 05029, South Korea

ARTICLE INFO

Handling Editor: Prof. A.I. Incecik

Keywords:
Flying-fish-inspired robot
Gliding
Tail-beating
Water-leaping
Head wind
Computational fluid dynamics

ABSTRACT

Mimicking the unpowered gliding capabilities of flying fish is challenging, due to the various technical limitations that are involved in creating a dual-modal robot that can both swim underwater and fly in the air. In this work, we suggest a modified KUFish design equipped with a pair of foldable wings for gliding flight in the air. Although the current water-leaping speed of the KUFish is lower than that of flying fish, the robot may be able to lift off by taking advantage of a head wind and forces produced by tail-beating motion, compensating for its weight, and overcoming the drag. Our series of computational fluid dynamics simulations has shown that with the unfolded wings and fully submerged tail-beating motion, when the wing and body angles are maintained in specific ranges under the head wind speeds of (9.5 and 6.5) m/s, the robotic fish after water-leaping can perform efficient gliding flight without generating pitching moment. This work can also be used to explain how flying fish perform gliding flight under tail-beating motion, and to develop an actual model of the dual-modal robot that mimics flying fish in the future.

1. Introduction

The studies of animal locomotion in nature over the past centuries provide valuable inspirations for developing robotic locomotion systems (e.g. swimming, jumping, crawling, and flying) (Mallock, 1928; Lock et al., 2013). Among many species exhibiting multi-modal behaviour, we are especially interested in the flying fish, which is a marine fish of the Exocoetidae family with unique aerial–aquatic transition capability. The studies of the flying fish in Breder (1929), Fish (1990), Davenport (1994), Park and Choi (2010), and Nelson et al. (2016) inspire researchers to develop robots that can fly after swimming, or swim after flying (Siddall and Kovač, 2014; Siddall et al., 2017; Zeng et al., 2022). As discussed in Davenport (1994), flying fish jump out of water with a speed of about 10.0 m/s, which is equivalent to (10−20) body lengths per second. After reaching a fast-swimming speed to exit the water surface, flying fish can effectively glide at relatively fast speed (Fish, 1990). When they completely leap out of the water, the flight efficiency of flying fish is due to unpowered gliding without flapping pectoral fins or beating tail.

Although the unique dual-modal locomotion of flying fish has drawn much attention from scientists, only a few studies have addressed the aerodynamic characteristics of flying fish models. For example, Park and Choi (2010) performed a series of wind-tunnel experiments to investigate the aerodynamic performance of the gliding flight for several real flying fish models (*Cypselurus hiraii*). For the experiments, to maintain the body and wing geometries, the bodies of the fish models were hardened through injecting urethane foam inside the body, while fully-spread wings were fixed. They confirmed that at an angle of attack (AoA) of around (30–35)°, their flying fish models weighing 0.6 N achieved the maximum lift coefficient (C_L) of about 0.78, while the maximum lift-to-drag ratios (L/D) were about 4.37 at an AoA of (−5 to 0)°. This agrees with the previous observations on the body angle of flying fish during leaping from the sea surface and performing gliding, in which the largest lift is required, as reported by Hertel (1966) and Davenport (1994). Inspired by this work, the aerodynamic characteristics of the artificially designed flying fish models, whose geometric parameters were designed based on the real flying-fish models tested in the wind-tunnel experiment by Park and Choi (2010), were numerically studied using the Spalart–Allmaras Delayed Detached Eddy Simulation model (SA−DDES) (Deng et al., 2019a). They reported that the maximum C_L of 1.03 is computed at an AoA of 35°, while the maximum L/D of 4.7 is obtained at an AoA of 6°. Also, they analyzed the longitudinal stability of the models by ranging the CG locations such that as the AoA increases, the slope of pitching moment is negative. To perform

* Corresponding author.
E-mail address: hcpark@konkuk.ac.kr (H.C. Park).

https://doi.org/10.1016/j.oceaneng.2023.115745
Received 23 February 2023; Received in revised form 18 July 2023; Accepted 29 August 2023
Available online 27 September 2023
0029-8018/

the taxiing on the sea surface, in Deng et al. (2019b), the hydrodynamics of the rigid beating and periodically morphing tails were investigated for variations of tail-beating frequencies from (80–200) Hz using the SST K–ω Detached Eddy Simulation model and Volume of Fraction (VOF) method to model the two-phase simulations. They concluded that under an inflow speed of 16.5 m/s, the requirement of minimum power for cruising is 350 W and the tail-beating frequency is 145 Hz, which is significantly greater than that of about 50 Hz based on the observation by Hertel (1966).

Recently, thanks to technological advancement, creating a robot that is able to perform dual-mode locomotion has become a feasible task, even though it is still challenging (Siddall and Kovač, 2014; Lock et al., 2013; Zufferey et al., 2019; Siddall et al., 2017; Zeng et al., 2022; Sihite et al., 2023). To mimic the gliding of flying fish, we first need to create a fish-like robot that can swim fast underwater, leap out of water, and perform water taxiing with relatively fast speed. For faster swimming, the body undulation needs to decrease, mimicking the thunniform fish (Salazar et al., 2018). Incidentally, the most noticeable robot using tail-beating mechanism is the iSplash−II (Clapham and Hu, 2015), which is the fastest swimming robot mimicking carangiform swimmers with the body undulation increasing toward the caudal tail fin area. In practice, the iSplash−II could reach an average maximum speed of 3.6 m/s (11.6 body lengths per second). Considering that this speed is the fastest swimming speed ever recorded by a tail-beating robotic fish (Clapham and Hu, 2015; Pham et al., 2023), it is evident that the water-leaping speed of real flying fish (~10.0 m/s) is too high to model. Therefore, creating a fish-like robot with a swimming speed of 10 m/s may be difficult due to many technical hurdles, including high power requirement (Gao and Techet, 2011; Deng et al., 2019b).

Flying fish do not always successfully perform such a complete jump out of water at high speed. Even though the water-leaping speed is lower than 10 m/s, they can manage to glide in the air by beating their tails, which remain underwater, as shown in Fig. 1a by Bamford (2016). Even if the flying fish jumps out of water into head winds with relatively lower water-leaping speed, it can still perform gliding flight by producing lift from its unfolded wings or pectoral fins, and thrust by its beating tail. As reported in Breder (1929), since flying fish tend to take off into the wind for unpowered gliding flight, while swimming underwater they may recognise pressure wave propagation above the water surface, and through water–air mixture created by the wind, to choose the water-leaping direction. The study also emphasised that the number of launches of flying fish into head wind is three times higher than that into downwind. This inspired us to generate a feasible design of the gliding flying-fish-like robot supported by tail-beating motion and study the required conditions to reproduce this unique flight mode of flying fish.

For the study, we used our previously developed robotic fish presented in Pham et al. (2023). Here, we only summarise the publication. The robotic fish, called KUFish, is propelled by a tail-beating pmechanism, driven by a DC motor. The mass of the KUFish is 116 g, and the body length is 160 mm. The robot was designed to make it swim fast underwater, leap out of water with a relatively high jumping speed, and stay in the air for a short time. In practice, the robot could perform fast swimming with a speed of about 1.4 m/s, and its body completely jump out of the water. At the instant of water leaping, the Froude number is about one. In this work, the anterior body is equipped with a pair of foldable wings. For underwater swimming, the wings should be folded, while after leaping out of the water, unfolded for gliding in the air. However, it is obvious that the KUFish may not create sufficient lift to compensate for the desired body weight of about 1.2 N, which is the weight of the robot equipped with two wings of about 6.4 g, at the take-off speed of 1.4 m/s. Therefore, for a gliding flight in air, the robot somehow needs to take advantage of a head wind, which is against the forward motion, even when the water-leaping speed is lower than 10 m/s. If the sum of the head wind speed and the water-leaping speed reaches the minimum take-off speed, the KUFish still has a chance of gliding. In this case, the thrust produced by underwater tail-beating motion may provide an additional vertical force to support the weight, and a reasonable thrust to overcome the drag. For such gliding flight, the pitching moment at the center of gravity (CG) must be zero for longitudinal static stability. Fig. 2 illustrates the potential procedure of the gliding flight of a flying-fish-like robot supported by the tail-beating motion after water-leaping of the body.

Taking these considerations into account, we perform a series of three-dimensional computational fluid dynamics (CFD) simulations using ANSYS−Fluent (ANSYS Inc, 2009) to analyze the wing and body aerodynamic and tail hydrodynamic characteristics. The numerical methods are widely used to investigate the hydrodynamic characteristics of the underwater swimmers (Suzuki and Kato, 2005; Liu et al., 2011; Borazjani, 2013; Tanaka et al., 2019; Deng et al., 2019a, 2019b; Han et al., 2020) and water-jumping fish (Mendelson and Techet, 2018; Khosronejad et al., 2020). The aerodynamic analyses assume the wings and body to be stationary during the gliding flight. Meanwhile, in the analyses of the tail, the tail-beating kinematics at a frequency of 9.1 Hz, which is measured in the tethered swimming test, is applied for the dual-media flow simulations. We assumed that the tail is fully submerged underwater during tail-beating motion for all body angles considered in this study, even after the body jumps out of water with an assumed speed of 1.5 m/s, which is slightly higher speed than that measured in Pham et al. (2023). To ensure the tail remains fully underwater during the tail-beating supported gliding flight, the peduncle length is extended to 35 mm from its original design of 18 mm, as reported in Pham et al. (2023). The gliding ability of the KUFish is first examined for a head wind speed of 9.5 m/s, corresponding to an effective inflow air speed of 11.0 m/s. The effect of head wind is also tested for lower speeds of (6.5 and 4.5) m/s, corresponding to the effective inflow air speeds of (8.0 and 6.0) m/s, respectively. The selected head wind speeds are within the actual wind speed range of the Indian Ocean (Kumar et al., 2013). After performing the numerical tests, the total vertical and horizontal forces, and pitching moments about the CG by the tail, wings, and body, are analyzed to identify the conditions under which the robot can perform a tail-beating supported gliding flight with the best gliding efficiency. The conditions are for a larger lift than the

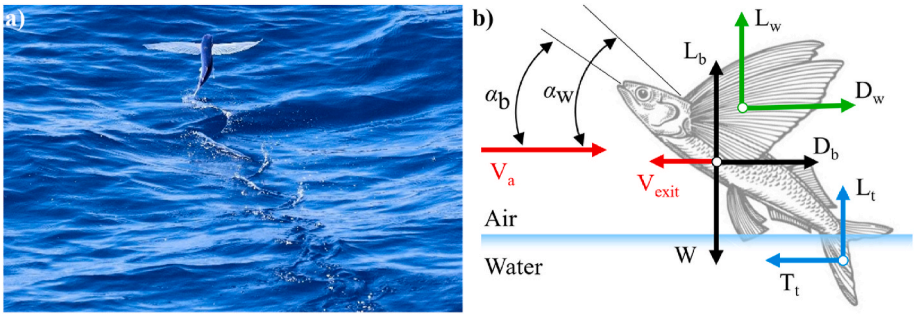

Fig. 1. a) Flying fish gliding supported by tail-beating (Bamford, 2016), and b) forces acting on the body.

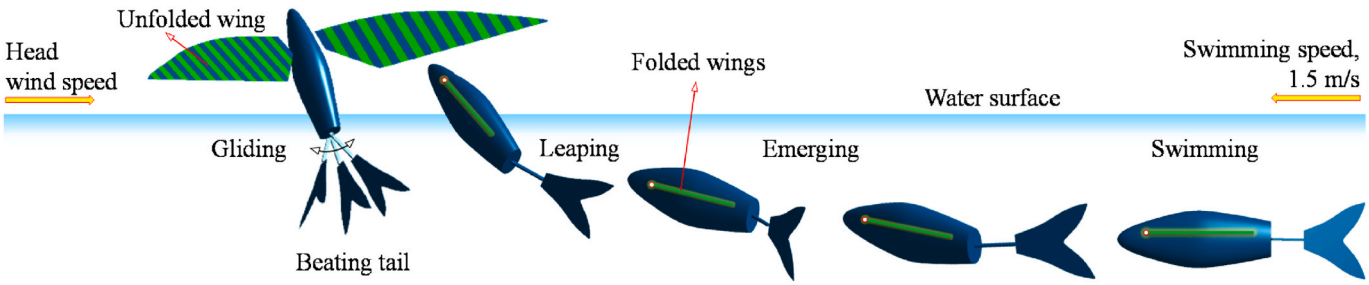

Fig. 2. Schematics of the gliding flight supported by the tail-beating motion of the KUFish.

total weight, a greater thrust than drag, and a zero-pitching moment about the CG.

This paper is constructed as follows: Section 2 defines the feasible morphological parameters of the modified KUFish, tail-beating kinematics, and CFD modelling of the wings, body, and tail, and also describes numerical estimations for the mean aerodynamic centers of the wing (AC_w) and body (AC_b), and the mean hydrodynamic center (HC) of the tail; it also explains the calculations of pitching moment about the CG (M_{CG}). Section 3 reports the computed aerodynamic forces by the wings and body, and hydrodynamic forces by the tail, and also analyses the effects of head winds on the gliding flight supported by tail-beating motion. Section 4 discusses the results, while Section 5 concludes the paper. Appendix A compares the aerodynamic characteristics of the KUFish with those of the real flying fish.

2. Materials and methods

2.1. Flying-fish-mimicking model of the KUFish

Fig. 3 defines the physical parameters of the KUFish with wings, while Table 1 lists their feasible values. The wings of the KUFish need to satisfy similar characteristics to those of the real flying fish, for example, wing shape, wing loading, and aspect ratio. The principles of wing design are explained as follows. Based on the findings of several real flying fish tested in Davenport (1994) and Fish (1990), Park and Choi (2010) plotted the allometric relationship between the wing loading and body length of fish models. As reported by Park and Choi (2010), the average body length of the studied adult flying fish varies from about (200–250) mm, corresponding to a wing loading of about (50–70) N/m^2. For our design, after extending the peduncle length, the total body length of the KUFish is 177 mm, which is close to the measured length of adult flying fish. Based on this, if we assume the total weight (W) is about 1.20 N, including the wing mass of 6.4 g, the area of our KUFish wings is suggested to be about 240 cm^2 to result in the wing loading of about 50 N/m^2. Since the wing area of the KUFish is about 10 times

Table 1
Morphological parameters of the KUFish model.

		Symbols	Unit	KUFish
Wing:	Aspect ratio	AR		9.4
	Mean chord length	c_{mean}	mm	50
	Lateral dihedral wing angle	β	degree	12
	Initial incidence angle of the wing	α_{w0}	degree	15
	One-wing length	l_w	mm	225
	Two-wing wetted area	S_w	cm^2	235.78
	Wingspan	S	mm	471.6
	Wing mass	m_w	g	6.4
Tail:	Length of peduncle	l_{pe}	mm	35
	Tail length	l_t	mm	65
	Tail height	h_t	mm	70
	Tail area	S_t	cm^2	22
Body:	Body length	l_b	mm	177
	Body mass	m_b	g	116
	Body wetted area	S_b	cm^2	211.0
	CG coordinate from the nose	z_{CG}/l_b		0.46
	CG coordinate below the longitudinal body axis	y_{CG}/h_t		0.073

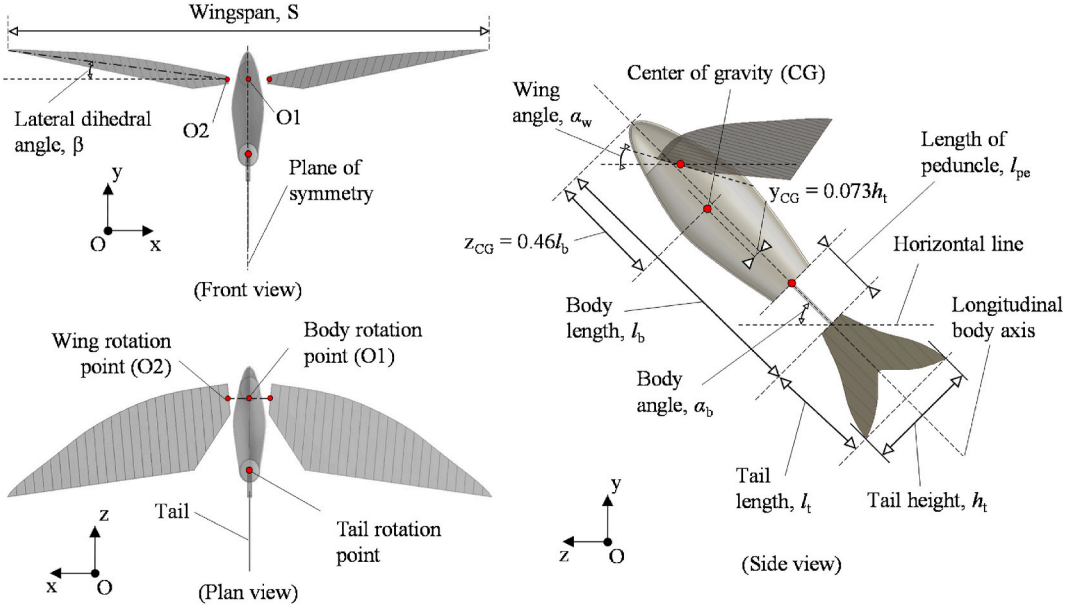

Fig. 3. Definitions of morphological parameters for the KUFish with wings.

greater than that of our flapping-wing robot, called KUBeetle (Phan et al., 2017), the mass of the two wings is estimated to be about 6.4 g by proportionally increasing the wing mass of the KUBeetle, of about 0.4 g, and adding more rigidity. However, to make the robot controllable, we expect more weight increase. Therefore, in Section 4, we later discuss the difference when the robot has a heavier total weight.

In addition, as discussed in Anderson (2009) and Bras et al. (2022), the wings with high AR are beneficial to reduce induced drag and improve longer flight endurance. Thus, the current wings of the KUFish have a relatively high AR of about 9.4, which is also in a similar range to that of birds (Fish, 1990; Withers, 1981). The wings are installed with a lateral dihedral wing angle (β) of 12°, and an initial incidence wing angle or angle of attack with respect to the horizontal line (α_{w0}) of 15°. Real flying fish were observed to adjust their wing angles during flights under certain conditions (Hubbs, 1933). Thus, the KUFish wings are designed to rotate about the pivot O2, which is slightly above and in front of the CG. Meanwhile, the body rotates about the pivot O1, which is a projected point of O2 on the plane of symmetry. After attachment of the wings and extension of the peduncle length, we expect that the CG remains unchanged from the location of the previous design by Pham et al. (2023), which is 0.46 l_b from the nose, and 0.073 h_t below the longitudinal body axis (see Table 1).

2.2. Measurement of the tail-beating kinematics and thrust prediction

The actual tail-beating kinematics are required for the CFD analysis to predict thrust generation by tail-beating motion. Fig. 4a presents the test setup used for measurement of the tail-beating kinematics without the yawing motion, while Fig. 4b shows an image recorded by a high-speed camera (Photron, Camfast Mini UX 50, Japan) taken from the top view. As evidenced by the experiment, the tail deforms along the length direction, while its flexibility along the height direction is insignificant. As shown in Fig. 4b, the tail is installed such that it rotates around the pivot point, at which the peduncle and body are connected.

To reconstruct the underwater tail-beating motion, the seven macros are marked at the hinge and other six locations along the tail length at (0, 0.2, 0.3, 0.5, 0.75, and 1.0) l_t. The MATLAB software package DLTdv8 (Hedrick, 2008) is used to manually digitise the locations of these points at each time step. In our previous studies, the same technology was successfully employed to track and fit the underwater free-swimming kinematics of the KUFish (Nguyen et al., 2022b), and the hovering wing kinematics of flapping-wing robots (Nguyen et al., 2021a; Au et al., 2020). To compute the tail-beating angles, θ is defined as the angle between the z–axis and the line, connecting the rotation axis and each macro marked on the tail. We use Eq. (1) to fit the measured angles over cycles at each macro:

$$\theta(t) = a_0 + \sum_{k=1}^{k=9}[a_k \cos(2k\pi ft) + b_k \sin(2k\pi ft)], \quad (1)$$

where the coefficients of a_0, a_k, and b_k are designated in the user-defined function in ANSYS−Fluent. Fig. 4c shows the measured and fitted beating angles at each location. Then, the spline interpolation method is used to interpolate the tail-beating angles along the tail length direction. Fig. 4d displays the underwater tail-beating motions reproduced in ANSYS−Fluent. The CFD results revealed that the cycle-average thrust generated by this tail-beating kinematics with a peduncle length of 18 mm is 0.97 N, which is 10% smaller than the measured thrust of 1.08 N reported in Pham et al. (2023). Therefore, the estimated thrust by the CFD is in good agreement with the measured thrust under the zero-inflow speed. More details on the CFD modelling and the results are available in Nguyen et al. (2022a).

In the current two-media (air and water) transient simulations, since the flow is very diffusive, the tail-beating cycle is redefined to begin at the middle of the stroke, corresponding to $t/T = 0.25$ of the tail-beating kinematics presented in Fig. 4d1 and 2, which makes the mesh around the tail symmetric. In this study, the measured tail-beating kinematics is applied to its fully-submerged tail-beating motion, as shown in Fig. 5 for

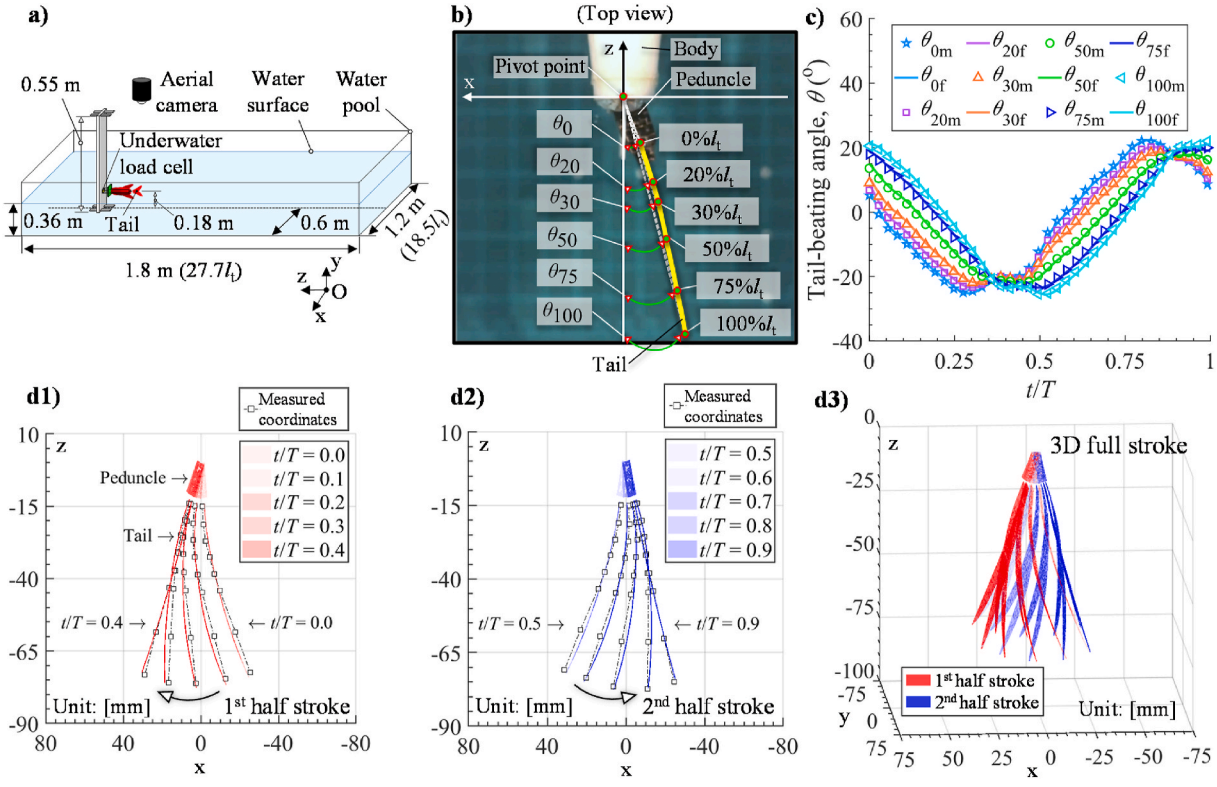

Fig. 4. Measurement of the underwater tail-beating kinematics: a) Experimental setups. b) Definitions of tail angles. c) Measured (m) and fitted (f) data. d) Tail-beating motions reproduced in the CFD.

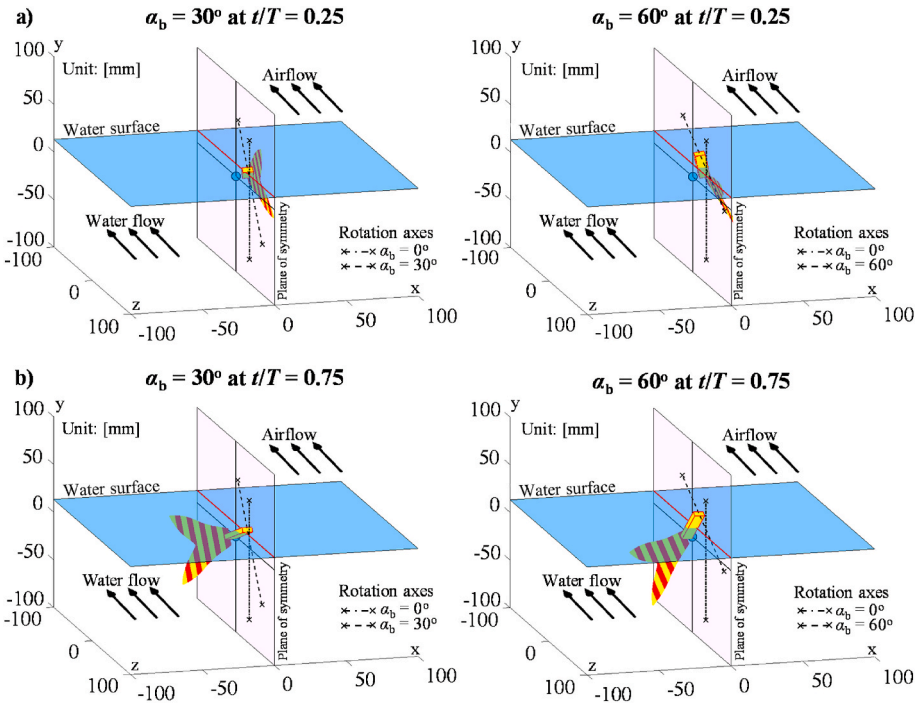

Fig. 5. Tail-beating motions for α_b = (30 and 60)° at a) t/T = 0.25, and b) t/T = 0.75.

the two body angles of (30 and 60)° tilted from the horizontal plane. The dashed lines on the vertical yz plane represent the rotation axes of the tail, while the horizontal solid red lines represent lines of intersection between the yz plane and the water surface.

2.3. Computational fluid dynamics (CFD) modelling

The simulations are independently performed for the aerodynamics of the wings and body, and for the hydrodynamics of the tail, whose modelling of the computational domains is shown in Fig. 6a and b, respectively. Since the effect of water–air interaction on the aerodynamic features of wings and body is assumed to be negligible, the wings and body are analyzed in the steady airflow condition. Meanwhile, since the composition of an air and water mixture is involved in the tail-beating simulation, we have applied the volume of fraction (VOF) method to model the water surface. To save computing time, the mesh in the far field region is stationary, whereas the dynamic mesh method is applied in the high-density region around the tail. For the simulations, we used a high-performance computer with 12th Gen Intel® Core™ i5-12,600 K 3.7 GHz × 16 processors. The Reynolds numbers, Re, of the tail, body, and wings are computed using Eq. (2):

$$\mathrm{Re} = \mathrm{V_{inflow}} \times l_{re} \times \upsilon^{-1}, \tag{2}$$

where $\mathrm{V_{inflow}}$ is the effective inflow air speed (11.0 m/s) for the wings and body, and the inflow water speed (1.5 m/s) for the tail, υ is the kinematic viscosity of the fluid at 20 °C (1.004×10^{-6} m^2/s for water, and 1.511×10^{-5} m^2/s for air), and l_{re} can be the reference lengths of the tail (l_t), and the body (l_b), and the mean chord of the wing (c_{mean}). Since Re is about 3.6×10^4 for the wing, 1.3×10^5 for the body, and 9.7×10^4 for the tail, the SST K–ω is designated to model the massively turbulent diffusion by the flow separation from the wings and body at high angles of attack, and the tail during tail-beating motion. For the tail simulation, the timestep, Δt is set to 1/1,000th of the tail-beating cycle to ensure the Courant number (Co) is smaller than one, satisfying the Courant–Friedrichs–Lewy (CFL) condition (Courant et al., 1928), $\mathrm{Co} = u\Delta t/\Delta h \leq 1$, where u is the local speed of fluids travelling across a local grid cell Δh in a unit of time Δt. Based on the Blasius solution for flat-plate turbulent flow (Schlichting, 1979), the boundary layer thickness, as denoted by δ_b in Eq. (3), is about 2.3 mm for the wing, and about 2.5 mm for the tail:

$$\delta_b = 0.38 \times l_{re} \times \mathrm{Re}^{-1/5}, \tag{3}$$

where l_{re} represents the lengths of the tail (l_t) and the wing (c_{mean}). To model the boundary layer of the wing, seven prismatic cell layers are grown from the wing surface with the first cell height (H_{1st}) of 0.2 mm, corresponding to Y^+ of about 9. To model the tail, since the shape is too complex to guarantee high quality of the first and last layers in terms of geometric orthogonality, only five layers are created within a half of the boundary layer thickness of 2.5 mm with the H_{1st} of 0.15 mm, corresponding to Y^+ of about 10. Even though the Blasius estimated solution is for the flat plate, the same H_{1st} and number of prismatic cell layers for the wings are set to the body for consistency. Equation (4), which is the formula of the geometric series (Moise, 1967; Riddle, 1970), is used to calculate the two dependent variables G and N, based on the H_{1st} for a desired Y^+:

$$\delta_b = H_{1st}\frac{1-G^N}{1-G}, \tag{4}$$

where δ_b is the boundary layer thickness estimated by the Blasius's solution, H_{1st} is the first cell height from the wall surfaces, G is the layer growth ratio, and N is the number of layers.

2.4. Mesh convergence study

The mesh convergence is validated by the two grid parameters (in milimeter): the maximum edge length of the triangular cells on the tail, wing, and body surfaces, l_1, and the maximum edge length of tetrahedral cells around the high-density region for tail and near-wall boxes for wings, l_2. For aerodynamic analyses, three cases of the grids 1, 2, and 3 are created to study the mesh convergence, and Table 2 shows their parameters. The lift ($C_{L,w}$ and $C_{L,b}$) and drag ($C_{D,w}$ and $C_{D,b}$) coefficients, and pitching moment coefficients about the CG ($C_{MCG,w}$ and $C_{MCG,b}$) are shown for $\alpha_w = 0°$ (corresponding to the effective wing angle of attack, $\alpha_{eff} = \alpha_w + \alpha_{w0} = 15°$) and $\alpha_b = 35°$ in Table 3. Equations (5)–(7) are used to define the C_L, C_D, and C_{MCG} for the wings and body, respectively:

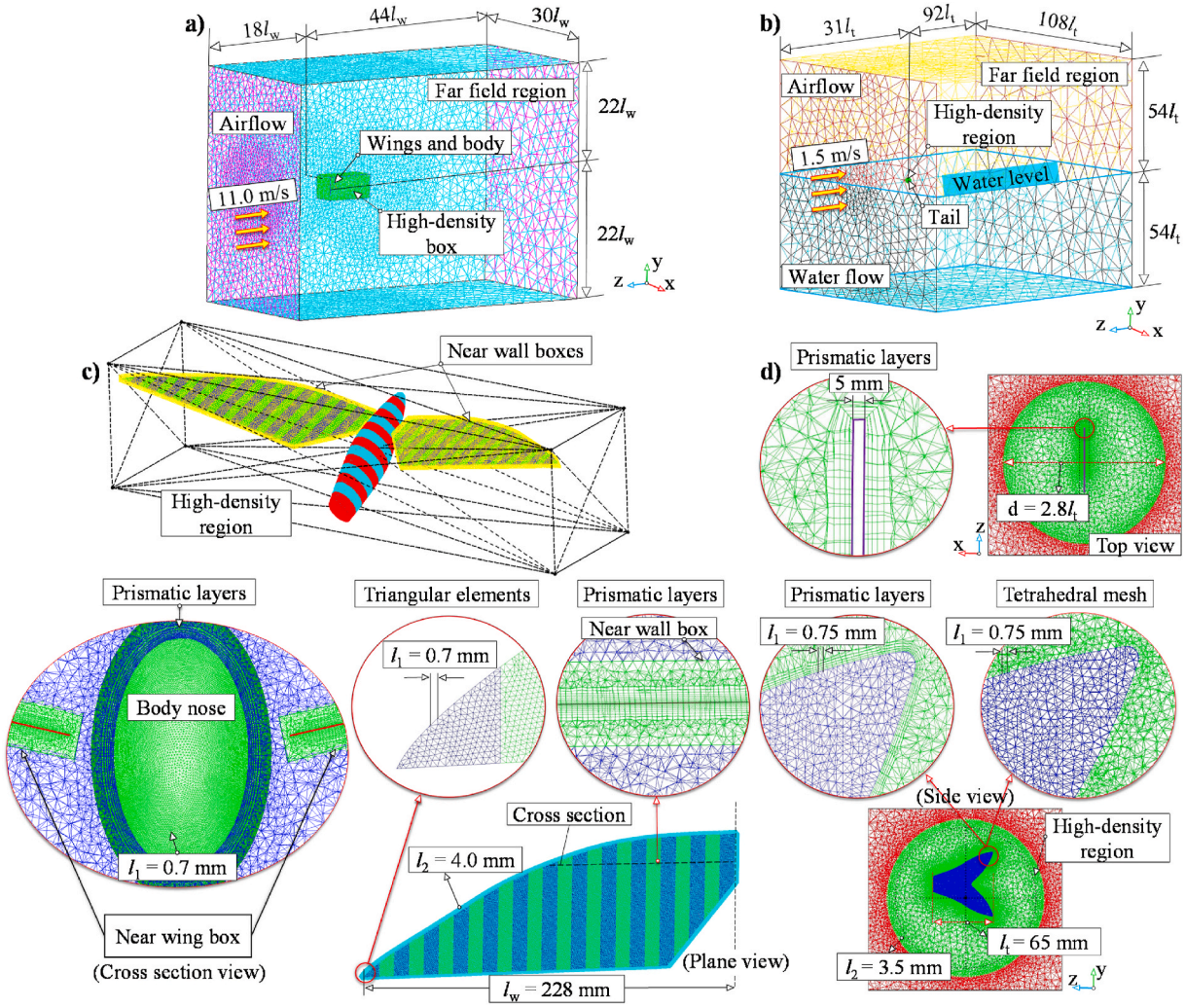

Fig. 6. Models of the computational domains for: a) the wings and body, and b) tail; and the mesh refinement around c) the wings and body, and d) tail.

Table 2
Grid information for the mesh convergence study of the wing simulation including wall layers.

Grid	Grid size (approx.)	N	G	H_{1st}	Y^+	$l_1 \times l_2$
1	4,273,000	6	1.224	0.30	~13.3	0.80 × 5.00
2	5,500,000	7	1.170	0.20	~9.0	0.70 × 4.00
3	8,171,000	9	1.224	0.10	~6.6	0.60 × 3.00

Table 3
Converged aerodynamic coefficients by the three grids for the wing angle α_w of 0° and body angle α_b of 35°.

Grid	$C_{L,w}$	$C_{L,b}$	$C_{D,w}$	$C_{D,b}$	$C_{M_{CG,w}}$ [a]	$C_{M_{CG,b}}$
1	0.740 (+1.1%)	0.061 (+1.7%)	0.206 (+1.5%)	0.048 (+2.1%)	0.0479 (+10.4%)	0.0080 (−8.0%)
2	0.735 (+0.4%)	0.060 (+0.0%)	0.205 (+1.0%)	0.047 (+0.0%)	0.0471 (+8.5%)	0.0085 (−2.3%)
3	0.732	0.060	0.203	0.047	0.0434	0.0087

[a] The calculations of pitching moment for the wing are based on the CG when $\alpha_b = 35°$ (see Subsection 2.5 for more details).

$$C_{L,w} = L_w/(0.5\rho V_a^2 S_w), \quad C_{L,b} = L_b/(0.5\rho V_a^2 S_b), \tag{5}$$

$$C_{D,w} = D_w/(0.5\rho V_a^2 S_w), \quad C_{D,b} = D_b/(0.5\rho V_a^2 S_b), \tag{6}$$

$$C_{M_{CG,w}} = M_{CG,w}/(0.5\rho V_a^2 S_w c_{mean}), \quad C_{M_{CG,b}} = M_{CG,b}/(0.5\rho V_a^2 S_b l_b), \tag{7}$$

where the subscripts "w" and "b" stand for wing and body, respectively. L, D, and M_{CG} are the lift, drag and pitching moment about the CG, respectively, ρ is the air density, V_a is the effective inflow air speed, and S_w and S_b are the wetted areas of the wings and body, respectively. Despite the significantly large difference of the total grid number, all desirable Y^+ values by the three grids are smaller than 14, as shown in Table 2, which results in three almost identical aerodynamic coefficients in Table 3. Thus, grid 2 is confirmed as the mesh that provides converged solutions for the aerodynamic simulations.

For the tail, the three meshes without prismatic layers, termed coarse grid 1, medium grid 2, and fine grid 3, are created for the mesh convergence study. Since the cycle-average forces of the 2nd and 3rd cycles are almost identical, the forces at the 2nd cycle are regarded as converged solutions (see Table 4). For the time courses in Fig. 7a, the forces by medium grid 2 show similar tendencies, compared to those by the finest grid 3, while the computing time for grid 2 is one day shorter.

Table 4
Grid information and cycle-average forces and moments for the case $\alpha_b = 30°$.

	Grid 1	Grid 2			Grid 3	Grid 4		
Layers	No	No			No	Yes (H_{1st} = 0.15 mm)		
$l_1 \times l_2$	1.0 × 4.0	0.75 × 3.5			0.5 × 3.0	0.75 × 3.5		
Size	712,232	1,632,503			2,523,119	1,776,228		
Y^+	20 − 30	20 − 30			20 − 30	< 10		
Time	2.0 days	3.0 days			4.0 days	3.0 days		
The cycle-average forces and moment at the second tail-beating cycle		$F_{z,t}$ (N)	$F_{y,t}$ (N)	$M_{CG,t}$ (Nm)		$F_{z,t}$ (N)	$F_{y,t}$ (N)	$M_{CG,t}$ (Nm)
		0.51 (+6%)	0.31 (−9%)	−0.001 (+83%)		0.48	0.34	−0.006

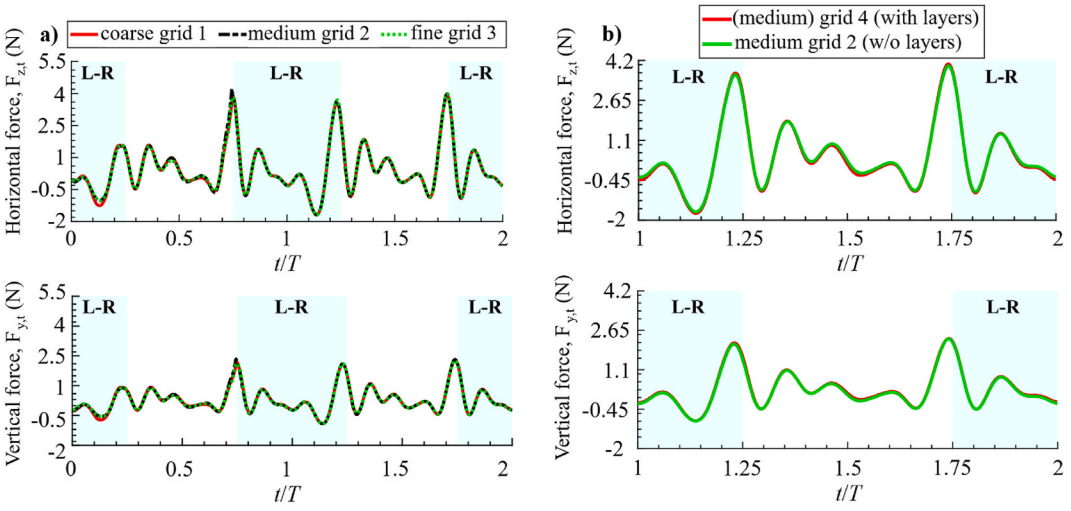

Fig. 7. Time courses of horizontal force $(F_{z,t})$ and vertical force $(F_{y,t})$ of the tail: for a) mesh convergence study, and for b) a comparison of forces by grids with and without prismatic layers.

Therefore, grid 2 is chosen to study the effect of the near-wall layers. However, since Y^+ of grids 2 and 3 is about (20–30) in Table 4, which is relatively high, we generate another grid 4, where five layers are included with the first cell height (H_{1st}) of 0.15 mm from the tail surface. The Y^+ of the tail with grid 4 is smaller than 10, which is (1.5–3.0) times lower than those of grids 2 and 3 without wall layers. Therefore, grid 4 is confirmed as the grid convergence for tail simulations. In addition, Fig. 7b compares the forces generated over the 2nd tail-beating cycle by

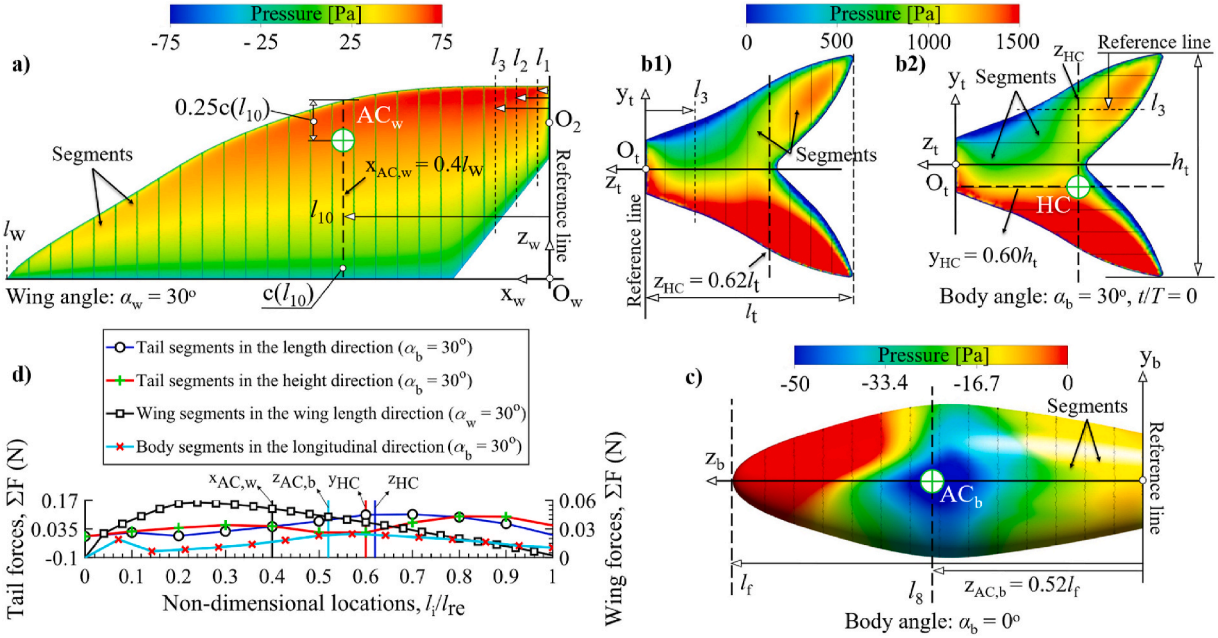

Fig. 8. Pressure distribution in the local coordinate systems on a) the wing surface ($\alpha_w = 30°$), and b1 and 2) the tail surface for two different divisions of segments ($\alpha_b = 30°$, $t/T = 0$), and c) the body surface ($\alpha_b = 0°$). d) Resultant force distributions of the wing, body, and tail along their non-dimensional locations, l_i/l_{re}.

grids 2 and 4. Grid 2 without layers (green line) shows higher $F_{z,t}$ but lower $F_{y,t}$, compared to the counterparts of grid 4 with layers (red line). Thus, the cycle-average results of grid 2 show a 6 % increase in $F_{z,t}$, a 9 % decrease in $F_{y,t}$, and about 80 % difference in the magnitude of $M_{CG,t}$, compared to those by grid 4, as shown in Table 4.

2.5. Estimation of aerodynamic center (AC), hydrodynamic center (HC), and pitching moment

Here, the locations of the ACs of the wing and body, and the HC of the tail are estimated as shown in Fig. 8a–c, since the pitching moment of the body significantly depends on the distances from the ACs and HC to the CG. Then, the derived equations for estimating the pitching moments of the wings and tail about the CG are presented as well. To find the ACs and HC, we performed quantitative simulations for different α_w and α_b. For the wing (Fig. 8a), since the wing AC in the chordwise direction is typically located at 25% of the local chord length from the local leading edge, we have not estimated the chordwise location of the AC. Meanwhile, in the spanwise direction, the wing is divided into 25 small segments of equal length. Similarly for the body, the AC is assumed to be on the symmetrical body axis. Therefore, 14 body segments are created along the longitudinal direction (Fig. 8c). However, for the tail (Fig. 8b1 and 2), due to different pressure distribution in the lower and upper parts when the inflow is passing by, the HC is not located at the central line of tail. Thus, 10 tail segments are divided in the tail's length and height directions to predict the location of HC in the z and y axes, (z_{HC} and y_{HC}), in Fig. 8b1 and 2, respectively. After computing the average forces produced by segments of the wing, body, and tail, the ACs and HC in their local coordinate systems are calculated using Eq. (8). This equation is also used to numerically identify the CG (Murray et al., 1967) and center of pressure, CP (Ordaz et al., 2015) of any object using the weight and pressure distribution, respectively, and segment centroids:

$$l = \frac{\sum_{i=1}^{i=n} F(i) \times l_i}{\sum_{i=1}^{i=n} F(i)}, \tag{8}$$

where l is the distance of the force center in each length direction measured from the reference line, n is the number of segments, F(i) is the average force of the ith segment, and l_i is the distance from the reference line to the ith-segment centroid. Fig. 8d shows the resultant forces of the wing and tail distributed along the local non-dimensional locations. Note that l_{re} in Fig. 8d is l_w to estimate the AC of the wing in the spanwise direction, l_f to compute the AC of the body in the longitudinal axis, l_t to locate the HC of the tail in the length direction, and h_t to find the HC of the tail in the height direction. Using Eq. (8), from the reference lines, the AC of the wing in the length direction is defined at 0.4 l_w (Fig. 8a). Meanwhile, the HC of the tail in the length direction (z_{HC}) is estimated as 0.62 l_t, while that in the height direction (y_{HC}) is located at 0.60 h_t from the reference lines (Fig. 8b). The AC of the body is at about 0.52 l_f from the reference length (Fig. 8c), (corresponding to 0.39 l_b from the nose). Then, these four locations are also represented by the vertical solid lines from left to right in Fig. 8d.

Fig. 9a shows the changes of the ACs, HC, and CG locations for various wing and body angles. After analyses, it is found that when the wing and body rotates, the ACs and HC in the local coordinate system do not vary much. However, in the global coordinate system, as shown in Fig. 9a, during the large rotations about the O1 and O2, they are significantly changed. To describe the rotations, the blue and green solid lines represent the longitudinal body and tail axes, respectively. The white circles illustrate changes in the AC locations for the wing angle variations, the yellow hexagrams represent the AC locations of the body, the cyan stars stand for shifts of the CG locations, the red squares indicate the rotated ends of peduncle, and the yellow diamonds represent the HC for the various body angles.

With the information, we can derive the equation of the pitching moment at the CG by following the method reported in Truong et al. (2014). In the derivation, we use the left-hand rule to define the positive pitching moment direction, as shown in Fig. 9b. In this case, the negative pitching moment is in the nose-down direction. The pitching moments of the wing $(M_{CG,w})$ and tail $(M_{CG,t})$ about the CG can be expressed as Eq. (9) for the wing, and Eq. (10) for the tail:

$$M_{CG,w} = M_{AC} + F_{y,w} \times (z_{AC} - z_{CG}) - F_{z,w} \times (y_{AC} - y_{CG}), \tag{9}$$

$$M_{CG,t} = M_{O,t} - F_{y,t} \times z_{CG} + F_{z,t} \times y_{CG}, \tag{10}$$

where the subscripts "w" and "t" stand for wing and tail, respectively, F_y is the vertical force, F_z is the horizontal force, and (y_{AC}, z_{AC}) and (y_{CG}, z_{CG}) are the y and z coordinates of the AC and CG, respectively. The forces produced by the wings in Eq. (9) are the converged ones, while those produced by the tail in Eq. (10) are the cycle-average ones. In Eq. (9), M_{AC} is the pitching moment about the AC by the two wings. Based on the pitching moment about the origin O, $M_{O,w}$, which is calculated by the CFD, we compute the M_{AC} using Eq. (11). Meanwhile, $M_{O,t}$ in Eq. (10) is the pitching moment about the origin O by the tail forces, which is computed using Eq. (12):

$$M_{AC} = M_{O,w} - 2\int_0^{l_w} z_P dF_{y,w} + 2\int_0^{l_w} y_P dF_{z,w}, \tag{11}$$

$$M_{O,t} = -\int_0^{l_t} z_Q dF_{y,t} + \int_0^{l_t} y_Q dF_{z,t}, \tag{12}$$

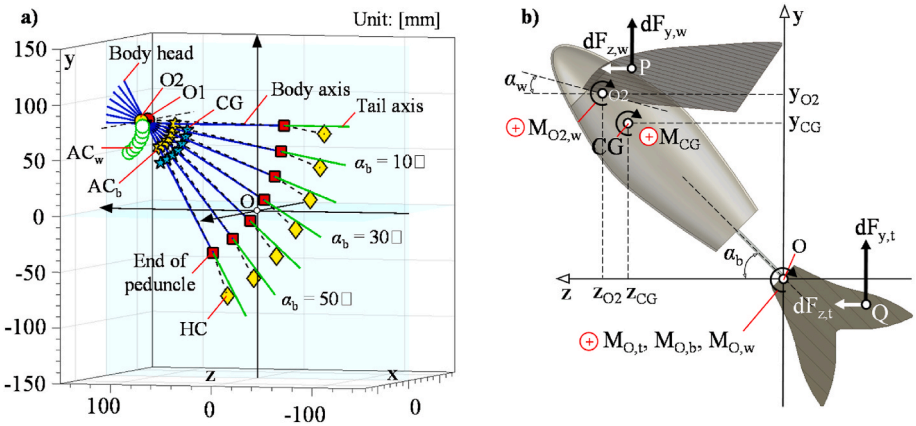

Fig. 9. a) Motion tracking during the wing and body rotations for the AC_b, AC_w, CG, and HC. b) Diagram of force and pitching moment components generated by the wing and tail.

where ($dF_{y,w}$ and $dF_{z,w}$) and ($dF_{y,t}$ and $dF_{z,t}$) are the force components decomposed in the y and z axes at arbitrary points P and Q on the wing and tail, respectively, as shown in Fig. 9b. Then, the M_{AC} and $M_{O,t}$ are expressed as Eqs. (13) and (14), respectively:

$$M_{AC} = M_{O,w} - F_{y,w} \times z_{AC} + F_{z,w} \times y_{AC}, \quad (13)$$

$$M_{O,t} = F_{y,t} \times z_{HC} - F_{z,t} \times y_{HC}, \quad (14)$$

where (y_{HC}, z_{HC}) are the coordinates of the HC. Finally, the pitching moment by the wings $(M_{CG,w})$ and that by the tail $(M_{CG,t})$ about the CG are expressed in Eqs. (15) and (16), respectively:

$$M_{CG,w} = M_{O,w} - F_{y,w} \times z_{CG} + F_{z,w} \times y_{CG}, \quad (15)$$

$$M_{CG,t} = -F_{y,t} \times (z_{CG} - z_{HC}) + F_{z,t} \times (y_{CG} - y_{HC}). \quad (16)$$

Similarly, for the body, the pitching moment about the CG $(M_{CG,b})$ is calculated by Eq. (17), while the sum of the pitching moments about the CG for the entire system (M_{CG}) can then be computed by Eq. (18):

$$M_{CG,b} = M_{O,b} - F_{y,b} \times z_{CG} + F_{z,b} \times y_{CG}, \quad (17)$$

$$M_{CG} = M_{CG,t} + M_{CG,b} + M_{CG,w}. \quad (18)$$

3. Results

3.1. Aerodynamic forces and moment from the wings

Since the body and wing rotations are implemented independently, Fig. 10a and b shows the lift and drag, and pitching moment coefficients of wing and body, respectively, for different angles of wing (α_w) and body (α_b). Meanwhile, Fig. 10c shows the L/D for wings and body. For more details, Table 5 presents the vertical (F_y) and horizontal (F_z) forces of the wings for four relatively low α_w values of (−10, 0, 10, and 20)°, and those of the body for four α_b values of (0, 20, 40, and 60)°. In addition, the pitching moment about the CG by the wings $(M_{CG,w})$ is analyzed for three α_b values of (20, 40, and 60)° with respect to four α_w values, while that by the body $(M_{CG,b})$ is presented for four α_b values of (0, 20, 40, and 60)°. Through the following discussions, the maximum wing angle α_w is set to 45° ($\alpha_{eff} = 60°$), since high α_{eff} is not beneficial for efficient flight in nature, which is also supported by our previous published study on the aerodynamic performance of the flapping wings (Nguyen et al., 2021b). Under Re of 10^4, flights with effective wing angle of attack greater than 50° make the L/D less than one. Meanwhile, the maximum body angle α_b is set to 60°, since the tail generates the smaller horizontal thrust for larger body angles. For the wings (Fig. 10a), the $C_{L,w}$ is almost zero at $\alpha_w = -15°$ ($\alpha_{eff} = 0$), and largest at about 20°, which is 0.76. Meanwhile, the minimum $C_{D,w}$ is close to zero at −15°, but for $\alpha_w > -10°$, as α_w increases, the C_D rapidly rises. For L/D (Fig. 10c), the wings have a relatively high L/D at α_w of (−10 to −5)°, which corresponds to (8.4–5.4), respectively. After that, the ratio becomes smaller than 1.0 when $\alpha_w > 30°$, which is poor for aerodynamic efficiency. For the body, due to the wing attachment location placed above the longitudinal axis and in front of the CG, the flow structures along the upper half of the body are affected (see Fig. 8c), which changes create the pressure difference between the lower and upper halves of the body. It is found that the airflow speed on the lower half is faster than that on its upper half, which interprets the negative lift production at $\alpha_b = 0°$ of $C_{L,b} = -0.03$ (Fig. 10a). Then, at $\alpha_b = 40°$, the body begins to stall, where maximum $C_{L,b}$ and $C_{D,b}$ are about 0.065. At $\alpha_b = 0°$, the $C_{D,b}$ is about 0.016. For α_b from (25–40)°, the $C_{D,b}$ is slightly smaller than $C_{L,b}$, which explains why for α_b from (25–40)°, the L/D is slightly larger than 1.0, as shown in Fig. 10c. This means that the current body fairing of the KUFish is not well-designed for high aerodynamic performance.

For the pitching moment coefficient, Fig. 10b shows the $C_{M_{CG,w}}$ for five body angles α_b with variations of wing angle α_w, and the $C_{M_{CG,b}}$ with different α_b. For the same α_b and small α_w, since the vertical and

Table 5
Aerodynamic forces and pitching moment of wings and body with several α_w and α_b values for $V_a = 11.0$ m/s.

1) For wings		(a1) $\alpha_w = -10°$	(a2) $\alpha_w = 0°$	(a3) $\alpha_w = 10°$	(a4) $\alpha_w = 20°$
$F_{y,w}$ (N)		0.640	1.266	1.369	1.538
$F_{z,w}$ (N)		−0.193	−0.353	−0.382	−0.425
$M_{CG,w}$ (Nm)	(b1) $\alpha_b = 20°$	0.016	0.023	0.023	0.025
	(b2) $\alpha_b = 40°$	0.012	0.015	0.015	0.015
	(b3) $\alpha_b = 60°$	0.005	0.002	0.001	−0.001
2) For body		(c1) $\alpha_b = 0°$	(c2) $\alpha_b = 20°$	(c3) $\alpha_b = 40°$	(c4) $\alpha_b = 60°$
$F_{y,b}$ (N)		−0.042	0.016	0.110	0.146
$F_{z,b}$ (N)		−0.001	−0.031	−0.092	−0.131
$M_{CG,b}$ (Nm)		−0.001	0.001	0.003	0.003

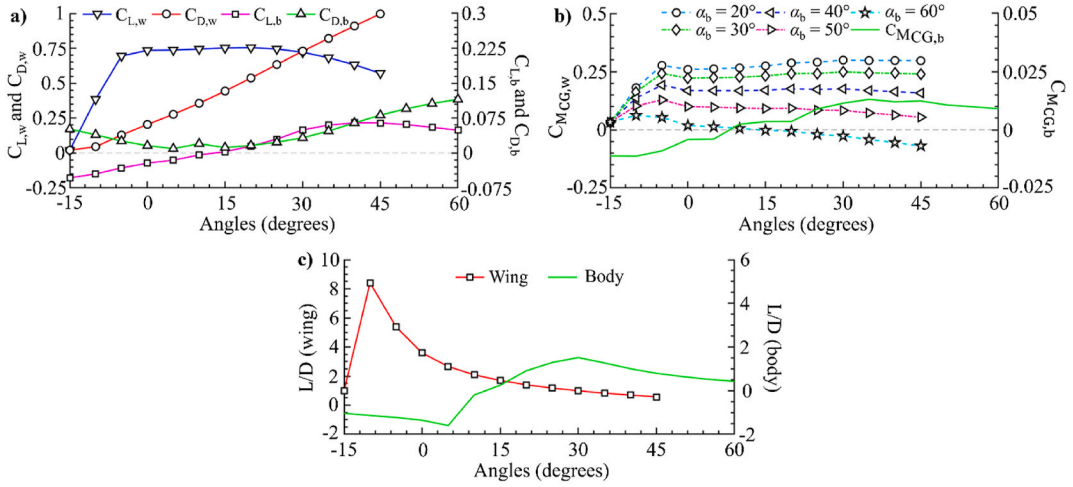

Fig. 10. Aerodynamic characteristics of the wings and body for different wing and body angles: a) coefficients of lift (C_L) and drag (C_D), and b) pitching moment coefficients about the CG of the wings $(C_{M_{CG,w}})$ for five different α_b values and of the body $(C_{M_{CG,b}})$. Positive $C_{M_{CG}}$ denotes a nose-up pitching moment, while negative means a nose-down pitching moment.

horizontal forces of the wings are small, and the CG is behind the AC, the wings generate the positive nose-up pitching moment. Then, as α_w increases, the AC moves further below the CG. In this case, the nose-up pitching moment is created by the larger $F_{y,w}$ and horizontal distance from AC to CG as α_w increases (see the second term in Eq. (9)). Therefore, this explains the increase in the $C_{M_{CG,w}}$ for α_b = (20 and 30)° in Fig. 10b and the $M_{CG,w}$ values for $\alpha_b = 20°$ in the row (b1) of Table 5, when α_w increases. For the same α_w and rising α_b, the nose-up pitching moment of the wings gradually reduces. The $C_{M_{CG,w}}$ curve of 40° is almost flat, since the CG becomes closer to the AC (see the second term in Eq. (9) and columns (a1−4), Table 5). The slope becomes negative for α_b of (50 and 60)° when the AC is in front of the CG. In this case, the vertical force $F_{y,w}$ generates the nose-down pitching moment together with the increase of negative M_{AC} as α_w increases. Similarly, for the body, the horizontal force $F_{z,b}$ is almost zero, while the vertical component $F_{y,b}$ is negative at $\alpha_b = 0°$ (column (c1), Table 5). Additionally, since the CG is behind the AC of the body, which is 0.39 l_b from the nose, the body produces the negative pitching moment even at $\alpha_b = 0°$, i.e., $M_{CG,b} = -0.001$ (Fig. 10b). However, when α_b rises, the force components also increase, which results in a production of positive nose-up pitching moment. This explains the trends of pitching moment generation of the wings and body by the independent rotations of the body and wings. To support the reliability of the current aerodynamic analysis by the CFD, we compare the computed coefficients with those of real flying in Appendix A.

3.2. Hydrodynamic forces and pitching moment from the tail

Fig. 11a and b illustrate the components of horizontal force $(F_{z,t})$ and vertical force $(F_{y,t})$, respectively, produced by the tail over the last two tail-beating cycles for five different α_b values. Due to the slight asymmetry of the tail-beating kinematics, the force generation values between two half-strokes in a cycle are not identical. However, the tendencies in each force component of the 2nd and 3rd cycles look similar. In addition, their cycle-average forces in Table 6 confirm that these results are almost identical. Thus, the forces in the 3rd cycle are considered as the converged solutions. When the body angles are changed from (20–60)° from the horizontal line, the peaks of $F_{z,t}$ become lower, whereas those of $F_{y,t}$ are higher, as shown in Fig. 11. More specifically, in Table 6, after reaching a highest value at $\alpha_b = 40°$ of 0.52 N, as α_b increases, the cycle-average $F_{z,t}$ reduces: at 50° of about 0.50 N, and at 60°, 0.45 N. Meanwhile, as α_b rises from (30–60)°, the cycle-average $F_{y,t}$ grows significantly from (0.35–0.95) N. Together with this characteristics, since the CG is in front of the HC, the tail produces the greater nose-down pitching moment $(M_{CG,t} < 0)$ when the body has the higher nose-up angles (Table 6).

3.3. Effect of head wind speed on the pitching moment

In this subsection, the effect of the head wind speed on the pitching moment about the CG is analyzed. The contour plots in Fig. 12a, b, and c show changes in the total pitching moment (M_{CG}), which is the sum of the pitching moments by the tail $(M_{CG,t})$ and by the wings $(M_{CG,w})$, under the effective inflow air speed of (11.0, 8.0, and 6.0) m/s, respectively. The effective inflow air speed is the sum of the head wind speed and the water leaping speed of the robot, which is 1.5 m/s. The total pitching moment in each case of a pair (α_b and α_w) is analyzed using the cubic interpolation method produced by MATLAB. The magenta curved lines between the two vertical lines in Fig. 12a, which are used to determine the minimum and maximum α_w, represent the gliding flight condition $(\Sigma F_y \geq W)$ and $(\Sigma F_z \geq 0)$ with $M_{CG} = 0$. The minimum α_w means the required wing angle to produce the minimum vertical force for take-off $(\Sigma F_y = W)$, while the maximum α_w indicates the maximum wing angle for gliding without thrust generation $(\Sigma F_z = 0)$ and $(\Sigma F_y \geq W)$. The areas in red colours stand for the nose-up pitching moment $(M_{CG} > 0)$, while those in blue colours indicate the nose-down pitching moment $(M_{CG} < 0)$. To clearly specify the possible gliding flight along the curved lines of $M_{CG} = 0$ in Fig. 12a–c, we search for the minimum α_w and α_b that make the total vertical force (ΣF_y) greater than the total weight, and total horizontal force (ΣF_z) positive at the same time. Along the curved lines of $M_{CG} = 0$, the squares indicate the minimum wing angles, the triangles show the maximum body angles, while the circles represent the maximum wing angles. Therefore, the magenta curved line between the two symbols of square and circle satisfies the conditions of gliding flight in terms of the vertical and horizontal forces and zero pitching moment. In general, when the effective inflow air speed reduces from (11.0–6.0) m/s, as shown in Tables 5 and 7, the vertical force generated by the wings $(F_{y,w})$ consequently becomes smaller, creating the smaller nose-up pitching moment $M_{CG,w}$. Meanwhile, the nose-down pitching moment by the tail $M_{CG,t}$ is not affected by the head wind. This explains that when the head wind speed reduces, the positive nose-up pitching moment M_{CG} becomes smaller for the same condition of α_w and α_b, especially for $\alpha_b < 40°$ in the two tables. As a result, the blue contour area $(M_{CG} < 0)$ moves from top to bottom (lower α_b), as the head wind speed reduces, as shown in Fig. 12a, b, and c.

The minimum wing and body angles required for gliding flight in each case are now discussed. For the effective inflow air speed $V_a = 11.0$ m/s in Fig. 12a, the range of α_w is limited from (−15 to 45)° for the curved line of $M_{CG} = 0$. When α_w increases from −15°, α_b should increase as well to make M_{CG} always zero. Specifically, the total vertical force ΣF_y required to lift the body is satisfied when $\alpha_w = -12.1°$ and $\alpha_b = 48.5°$, which corresponds to the minimum wing angle condition (denoted by the white square in Fig. 12a) of $\Sigma F_y = 1.21$ N, $\Sigma F_z > 0$. Similarly, for $V_a = 8.0$ m/s, the minimum conditions that match the requirement of $\Sigma F_y = 1.20$ N and $\Sigma F_z > 0$, happen at $\alpha_w = -6.3°$ and $\alpha_b = 43°$. However, for $V_a = 6.0$ m/s, the vertical force by the wings and body significantly drops compared to those of the two previous cases (comparing $F_{y,w}$ and $F_{y,b}$ for each case of V_a in Tables 5 and 7). In this case, within the investigated range of α_w and α_b, the robot produces the maximum ΣF_y of about 0.94 N, which is 22% smaller than the current total weight of 1.20 N. In addition, the magnitudes of horizontal forces

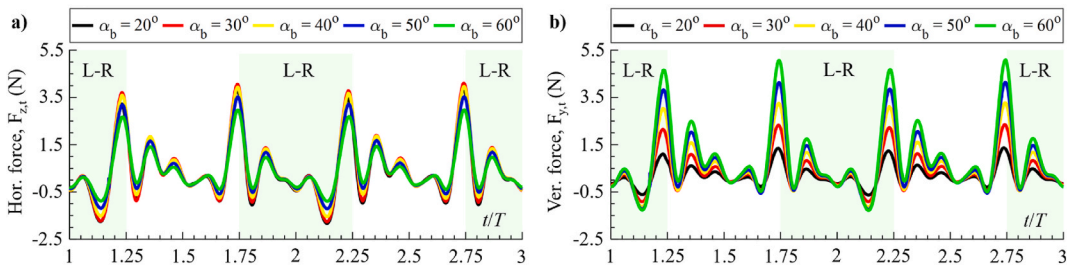

Fig. 11. Time courses of the a) horizontal force $(F_{z,t})$, and b) vertical force $(F_{y,t})$, for different body angles (α_b) over the last two tail-beating cycles. L−R stands for the left-to-right beating motion.

Table 6
The cycle-average forces and pitching moment of the tail with different body angles from (30–60)°.

t/T	(a) $\alpha_b = 30°$			(b) $\alpha_b = 40°$			(c) $\alpha_b = 50°$			(d) $\alpha_b = 60°$		
	$F_{y,t}$ (N)	$F_{z,t}$ (N)	$M_{CG,t}$ (Nm)	$F_{y,t}$ (N)	$F_{z,t}$ (N)	$M_{CG,t}$ (Nm)	$F_{y,t}$ (N)	$F_{z,t}$ (N)	$M_{CG,t}$ (Nm)	$F_{y,t}$ (N)	$F_{z,t}$ (N)	$M_{CG,t}$ (Nm)
1st	0.26	0.40	−0.003	0.38	0.36	−0.007	0.67	0.47	−0.008	0.85	0.40	−0.009
2nd	0.34	0.48	−0.006	0.53	0.52	−0.008	0.72	0.50	−0.009	0.94	0.45	−0.009
3rd	0.35	0.49	−0.007	0.54	0.52	−0.009	0.73	0.50	−0.010	0.95	0.45	−0.010

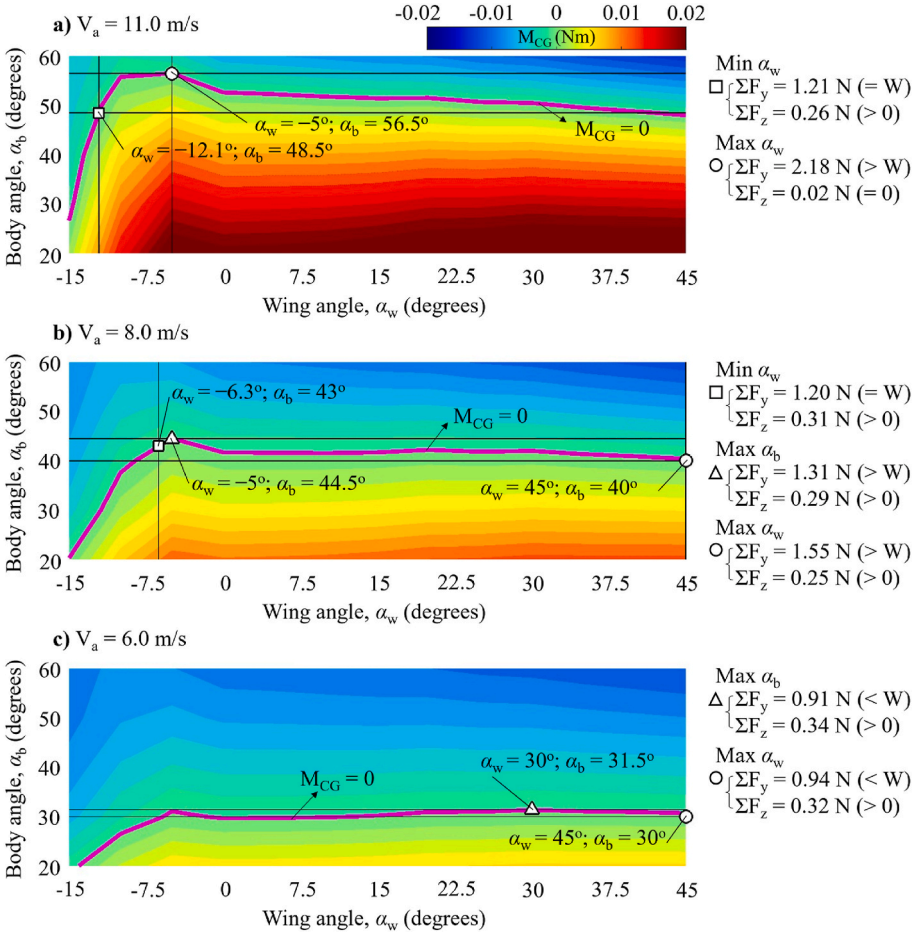

Fig. 12. Contour plots of M_{CG} with variations of the wing and body angles for the effective inflow air speed, V_a of a) 11.0 m/s, b) 8.0 m/s, and c) 6.0 m/s. The magenta contour lines indicate $M_{CG} = 0$.

generated by wings and body witness a considerable drop even at high α_w (comparing $F_{z,w}$ and $F_{z,b}$ in Tables 5 and 7), resulting in an increase in the ΣF_z, since the tail thrust generation is unchanged. More specifically, at $\alpha_w = 45°$, the robot produces 28% greater ΣF_z than that for $V_a = 8.0$ m/s (comparing (0.32 and 0.25) N in Fig. 12b and c, respectively), and may result in a faster gliding speed than for $V_a = 11.0$ m/s. Overall, to perform gliding flight when $V_a = 6.0$ m/s, the α_w and α_b should increase to greater than (45 and 31.5)°, respectively, since the current maximum ΣF_y is insufficient to compensate for the total weight of 1.20 N.

In terms of aerodynamic efficiency of the wings, for V_a of (11.0 and 8.0) m/s, the L/D are (5.3 and 6.2) at $\alpha_w = (-12.1$ and $-6.3)°$, respectively, from Fig. 10c. Meanwhile, for $V_a = 6.0$ m/s, to perform gliding flight, the α_w should increase to be greater than 45°. That means that the L/D is smaller than 0.57, which is about (89 and 91) % smaller than those for V_a of (11.0 and 8.0) m/s, respectively. Consequently, the effective inflow air speed of 6.0 m/s is not considered as a sufficient condition for gliding, since increasing the higher wing angle is not beneficial for the L/D. This also agrees with the findings reported in Latimer-Needham (1951), Hertel (1966), and Davenport (1994): for the best gliding performance, the bodies of flying fish in nature are observed almost parallel to the sea surface. Hence, under the condition of $\alpha_w = -6.3°$, $\alpha_b = 43°$, and $V_a = 8.0$ m/s, the KUFish weighing about 1.20 N can effectively glide with zero pitching moment and relatively high L/D of about 6.2. Moreover, the gliding speed will be faster, since the ΣF_z is about 19% greater than that for $V_a = 11.0$ m/s (comparing (0.31 and 0.26) N, in Fig. 12b and a, respectively).

4. Discussion

In the current work, the target weight (W) of the KUFish is 1.20 N. Then, the question arises: if the W is greater than 1.20 N, how heavy can the robot be and still glide? The robot can be heavier, since we expect to install a control system and possibly stiffer or heavier wings to the robot. Still, a heavier KUFish can perform gliding flight supported by a tail-beating motion. For this case, the ΣF_y generated by the wings and tail needs to be enhanced, while the ΣF_z still remains positive. To answer this question, we selected several cases to discuss, as denoted by the triangle and circle in Fig. 12a and b. For example, in the data set of 11.0

Table 7
Aerodynamic forces and pitching moments of wings and body with several α_w and α_b for V_a = (8.0 and 6.0) m/s.

(A) V_a = 8.0 m/s		(a1) $\alpha_w = -10°$	(a2) $\alpha_w = 0°$	(a3) $\alpha_w = 10°$	(a4) $\alpha_w = 20°$
For wings					
$F_{y,w}$ (N)		0.339	0.670	0.724	0.813
$F_{z,w}$ (N)		−0.102	−0.187	−0.202	−0.225
$M_{CG,w}$ (Nm)	(b1) $\alpha_b = 20°$	0.008	0.012	0.012	0.013
	(b2) $\alpha_b = 40°$	0.006	0.008	0.008	0.008
	(b3) $\alpha_b = 60°$	0.003	0.001	0.000	0.000
For body		(c1) $\alpha_b = 0°$	(c2) $\alpha_b = 20°$	(c3) $\alpha_b = 40°$	(c4) $\alpha_b = 60°$
$F_{y,b}$ (N)		−0.022	0.008	0.058	0.077
$F_{z,b}$ (N)		−0.001	−0.016	−0.049	−0.069
$M_{CG,b}$ (Nm)		−0.001	0.001	0.002	0.001
(B) V_a = 6.0 m/s		(a1) $\alpha_w = -10°$	(a2) $\alpha_w = 0°$	(a3) $\alpha_w = 10°$	(a4) $\alpha_w = 20°$
For wings					
$F_{y,w}$ (N)		0.190	0.377	0.407	0.458
$F_{z,w}$ (N)		−0.057	−0.105	−0.114	−0.126
$M_{CG,w}$ (Nm)	(b1) $\alpha_b = 20°$	0.005	0.007	0.007	0.008
	(b2) $\alpha_b = 40°$	0.004	0.004	0.004	0.005
	(b3) $\alpha_b = 60°$	0.002	0.000	0.000	0.000
For body		(c1) $\alpha_b = 0°$	(c2) $\alpha_b = 20°$	(c3) $\alpha_b = 40°$	(c4) $\alpha_b = 60°$
$F_{y,b}$ (N)		−0.012	0.005	0.033	0.043
$F_{z,b}$ (N)		0.000	−0.009	−0.027	−0.039
$M_{CG,b}$ (Nm)		0.000	0.000	0.001	0.001

m/s (Fig. 12a), along the curve of $M_{CG} = 0$, if α_w increases to −5° and α_b rises to 56.5°, which is denoted by the circle, a 82% heavier robot (W ≈ 2.18 N) can take off. Clearly, the higher α_w and α_b create the greater vertical force, resulting in the total vertical force ΣF_y of 2.18 N. However, the high α_w also produces greater negative $F_{z,w}$ (see Tables 5 and 7), while the high α_b (> 40°) generates smaller positive $F_{z,t}$ (Table 6) and greater negative $F_{z,b}$ (Tables 5 and 7), which explains why the $\Sigma F_z = 0$ N. This means that the robot cannot move forward since the ΣF_z is almost zero, which corresponds to the maximum condition to overcome the drag from wings and body. Similarly, for V_a = 8.0 m/s, the robot with a weight of 1.55 N (29% heavier) can glide, when the values of $\alpha_w = 45°$ and $\alpha_b = 40°$ are chosen to satisfy $M_{CG} = 0$, which is represented by the circle in Fig. 12b. This combination produces ΣF_y = 1.55 N and ΣF_z = 0.25 N, which is 19% smaller than ΣF_z = 0.31 N in the case of W = 1.20 N. Overall, for the two cases of (11.0 and 8.0) m/s, the KUFish with the heavier weight of about (2.2 and 1.6) N, respectively, can take off, and glide through the air by modifying α_w and α_b. However, the gliding flight with large α_w and α_b can create high ΣF_y but small ΣF_z, which reduces the forward speed. Here, the L/D should be considered again. Since the maximum wing angle α_w is −5° when V_a = 11.0 m/s (Fig. 12a), the L/D is slightly larger, at about 5.4. Meanwhile, for V_a = 8.0 m/s, the α_w is 45° (Fig. 12b), corresponding to the L/D of about 0.57, which is 89% smaller than that for V_a = 11.0 m/s. Clearly, the higher the angle at which the wings fly, the more L/D reduces (Fig. 10c). Thus, if the KUFish has a heavier weight of 2.18 N, under the condition of $\alpha_w = -5°$, $\alpha_b = 56.5°$, and V_a = 11.0 m/s, the robot can glide with a L/D of about 5.4.

The exact body angle of real flying fish during the gliding supported by tail-beating motion (or water surface taxiing) is not reported in the literature. Some reported that the maximum lift coefficient happens at the body angles of about (30–35)° (Park and Choi, 2010; Deng et al., 2019a). However, this body angle might be for the real flying fish, weighing about (0.50–0.60) N, when they completely exit the water surface with the observed exit speed of about 10 m/s or higher. We may roughly guess the body angle from the video on flying fish broadcasted through the video by BBC Earth (2017). The body angles seem to be more or less than 45° with respect to the horizontal line. As discussed above, the body angles need to increase to have the additional vertical force from tail-beating motion, and lift up the heavier body weight of 1.20 N. Therefore, the feasible body angle ranges that we found in Fig. 12 are close to those observed in the video.

The suggested wing shape here is not a fixed design. Once the constraints of wing loading, wing aspect ratio, and wing area are within the desired ranges, the final wing shape can be modified for more efficient flight. We may eventually vary the wing shape such that it is suitable for a wing folding and unfolding mechanism for future fabrication. Then, we may be able to find other conditions for a new wing design. Moreover, since the maximum wing and body angles considered in this work are limited at 45° and 60°, respectively, the current design margin is not that wide in the case of low head wind speed. If we have to trade-off the forward speed to achieve larger vertical force to compensate for a heavier weight in the low head wind speed, the α_w needs to be greater than 45° and the α_b should be greater than that in the considered maximum condition. As discussed before, the tail beating with higher α_b and the wings flying with greater α_w can produce greater vertical force. In this case, the tail creates a smaller positive force in the horizontal direction, while the wings and body produce the greater negative ones. To overcome this situation, we may improve the tail-beating thrust. With these strategies, we can widen the design margin for the possible gliding flights of the KUFish, even under low head wind speeds.

5. Conclusion

Inspired by the amazing tail-beating supported gliding flight of flying fish, we have suggested a robotic fish design that can perform gliding flight even when the water-leaping speed is lower than the required speed for complete water leaping and gliding, as observed in real flying fish. To create the design, we have performed a series of numerical simulations and identified the conditions for producing sufficient lift by wings to efficiently compensate for the total weight, thrust by tail-beating motion to overcome drag and provide additional vertical force, and to satisfy zero-pitching moment. We have also found that the design margins of the wing and body angles are large enough to accommodate up to 82% weight increase for the effective inflow air speed of 11.0 m/s, and up to 29% weight increase for the inflow air speed of 8.0 m/s. Thus, even when the KUFish becomes heavier, it is able to glide with a different set of wing and body angles for these two cases. Meanwhile, for the air flow speed of 6.0 m/s, the current KUFish cannot take off within the investigated range of the wing and body angles. Still, when the wing and body angles increase, the robot may have a chance to lift off. However, for high gliding efficiency, the lower wing angles are recommended for all inflow air speeds. The current work can also be used to explain how the flying fish can perform gliding supported by the tail-beating motion against head winds. On the other hand, many hurdles are expected in the actual fabrication of a controllable gliding robotic fish equipped with foldable wings. Also, the robot may experience dynamic motion due to the underwater tail-beating motion. Therefore, we need to extend the current feasibility study based on static analysis to dynamic analysis including wing flexibility. We leave these tasks for our future work.

CRediT authorship contribution statement

Khanh Nguyen: Conceptualization, Methodology, Data curation, Formal analysis, Writing – original draft, Visualization, Validation, Software, Investigation, Writing – review & editing. **Hoon Cheol Park:** Supervision, Conceptualization, Validation, Investigation, Resources, Writing – review & editing, Project administration, Funding acquisition.

Declaration of competing interest

The authors declare that they have no known competing financial interests or personal relationships that could have appeared to influence the work reported in this paper.

Data availability

The data that has been used is confidential.

Acknowledgement

This research was supported by a National Research Foundation of Korea (NRF) grant, funded by the Korea government (MSIT) (NRF-2020R1F1A106827212).

Appendix A. Validation of simulation results.

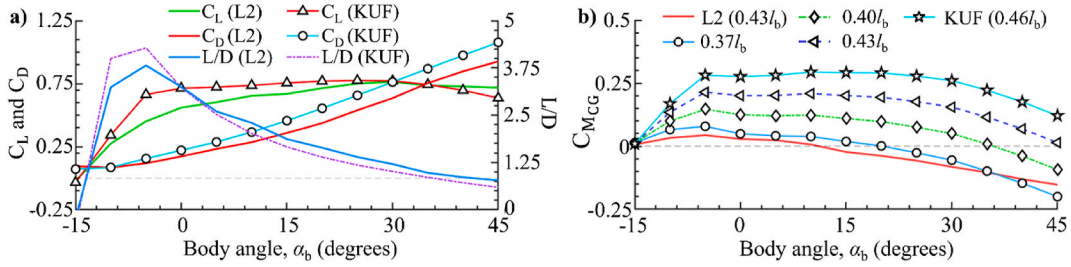

Fig. A1. Comparison of a) lift (C_L) and drag (C_D) coefficients, and b) pitching moment coefficient ($C_{M_{CG}}$), for the L2 model and for the KUFish (KUF) with various α_b. The $C_{M_{CG}}$ plot of the KUFish is shown for different CG locations. The results from the L2 model are extracted from Figs. 5 and 6 in Park and Choi (2010).

For validation of the aerodynamic results by the current CFD simulation, the computed coefficients of lift, drag, and pitching moment (C_L, C_D, and $C_{M_{CG}}$, respectively) of the KUFish are compared with those of the real flying fish, called the L2 model, which are measured in the wind tunnel under the inflow airspeed of 12.0 m/s (Park and Choi, 2010). Since the pectoral fins of the L2 model are fixed with an incidence angle of 15° from the longitudinal body axis, just as in our KUFish, we select the L2 model for comparison. Note that the aerodynamic coefficients of the L2 model are measured for the entire model including the body and pectoral and pelvic fins, while for the KUFish, only the wings and body are included in the calculation. Fig. A1–a compares the current computed and their measured coefficients for various body angles α_b. Generally, the current C_L and C_D show similar tendencies to those of the real flying fish. The small difference may be due to the difference in the wing shape. Meanwhile, the difference in $C_{M_{CG}}$ may be due to the difference in the CG and wing attachment locations.

For more details, the two C_L curves in Fig. A1–a do not show a sharp drop even after stall, which is similar to the characteristics of thin airfoils with sharp leading edges at low Re flow, found by McCullough and Gault (1951). In Table A1–a, the maximum C_L is 0.77 at α_b from (20–30)° for the KUFish, and the same maximum C_L for the L2 model is at 30°, when rounded to two decimal places. In Table A1–b, the C_D at $\alpha_b = -15°$ is 0.07 for the KUFish, while that of the L2 is 0.09. The two slopes of C_D curves look similar for $\alpha_b > 7°$, as shown in Fig. A1–a, which explains the similar slope of L/D for $\alpha_b > 7°$, after reaching the highest values of L/D at −5° for both models. For $C_{M_{CG}}$, the CG location of L2 model is at about 0.43 l_b from the nose, while that of the KUFish is further, at 0.46 l_b from the body head. Therefore, this longer distance from the wing AC to CG may generate the greater nose-up moments for KUFish (represented by the cyan solid line with pentagrams) than those for the L2 model (represented by red solid line), as shown in Fig. A1–a. Based on this, the pitching moment coefficients of the KUFish are analyzed for different CG locations. As shown in Table A1–c, the $C_{M_{CG}}$ witnesses a gradual reduction in positive magnitude and becomes negative when the CGs are moved closer to the nose from (0.46–0.37) l_b for the same α_b. Also, this reveals that when the CG is located at 0.37 l_b from the nose and α_b increases to be greater than 20°, the KUFish produces the negative nose-down pitching moment (Table A1 and Fig. A1–b). Meanwhile, the L2 model creates the pitch-down moment when $\alpha_b > 13°$ (Fig. A1–b). Thus, although there are geometric differences in the two models, the current aerodynamic coefficients computed by the CFD show similar tendencies to those of the flying fish measured by the experiment.

Table A1
Comparison of C_L, C_D, and $C_{M_{CG}}$ coefficients for the L2 and KUFish models for different body angles.

	α_b	−15°	−10°	0°	10°	20°	30°	40°	45°
a) C_L	L2 model	−0.02	0.27	0.56	0.65	0.71	0.77	0.73	0.72
	KUFish	−0.03	0.34	0.71	0.74	0.77	0.77	0.70	0.64
b) C_D	L2 model	0.09	0.08	0.17	0.28	0.44	0.63	0.85	0.93
	KUFish	0.07	0.09	0.22	0.37	0.55	0.76	0.97	1.08
c) $C_{M_{CG}}$	α_b	−15°	−10°	0°	10°	20°	30°	40°	45°
L2 model	CG at 0.43 l_b	0.006	0.033	0.028	0.007	−0.038	−0.082	−0.131	−0.153
KUFish	CG at 0.37 l_b	0.013	0.066	0.049	0.038	0.001	−0.055	−0.147	−0.200
	CG at 0.40 l_b	0.012	0.100	0.125	0.124	0.097	0.050	−0.039	−0.093
	CG at 0.43 l_b	0.011	0.134	0.200	0.209	0.194	0.155	0.068	0.014
	CG at 0.46 l_b	0.009	0.169	0.276	0.294	0.291	0.260	0.176	0.121

As a way to validate the CFD results of the tail, we may recall the estimated thrust based on the measured tail-beating kinematics with the original peduncle length of 18 mm under the zero-inflow-speed conditions in Section 2.2. The estimated thrust is about 10% smaller than the measured thrust. In addition, as the peduncle length increases by a small amount, we could observe during our experiments that the thrust production tends to increase.

Unfortunately, it is difficult to measure the net thrust under non-zero inflow condition. As a reason, the CFD results of the tail can be validated only by the case with zero inflow speed.

References

Anderson, J.D., 2009. Fundamentals of Aerodynamics. McGraw.

ANSYS Inc, 2009. ANSYS FLUENT 12.0, Theory Guide.

Au, L.T.K., Phan, H.V., Park, S.H., Park, H.C., 2020. Effect of corrugation on the aerodynamic performance of three-dimensional flapping wings. Aero. Sci. Technol. 105, 106041 https://doi.org/10.1016/j.ast.2020.106041.

Bamford, M., 2016. Photo of the Flying-Fish Flight. www.flickr.com/photos/mfmb_bentley/26249710934/in/photolist-FZACx1-FZGBTJ.

BBC Earth, 2017. Flying Fish Picked of from above and below. The hunt. BBC Earth. https://www.youtube.com/watch?v=bk7McNUjWgw.

Borazjani, I., 2013. The functional role of caudal and anal/dorsal fins during the C-start of a bluegill sunfish. J. Exp. Biol. 216 (9), 1658–1669. https://doi.org/10.1242/jeb.079434.

Bras, M., Warwick, S., Suleman, A., 2022. Aeroelastic evaluation of a flexible high aspect ratio wing UAV: numerical simulation and experimental flight validation. Aero. Sci. Technol. 122, 107400 https://doi.org/10.1016/j.ast.2022.107400.

Breder, C.M., 1929. Field Observations on Flying Fishes: a Suggestion of Methods. New York Zool. Soc.

Clapham, R.J., Hu, H., 2015. iSplash: Realizing Fast Carangiform Swimming to Outperform a Real Fish. Robot Fish, pp. 193–218. https://doi.org/10.1007/978-3-662-46870-8_7.

Courant, R., Friedrichs, K., Lewy, H., 1928. Über die partiellen Differenzengleichungen der mathematischen Physik. Math. Ann. 100, 32–74. https://doi.org/10.1007/BF01448839 (in German).

Davenport, J., 1994. How and why do flying fish fly? Rev. Fish Biol. Fish. 4 (2), 184–214. https://doi.org/10.1007/BF00044128.

Deng, J., Zhang, L., Liu, Z., Mao, X., 2019a. Numerical prediction of aerodynamic performance for a flying fish during gliding flight. Bioinspiration Biomimetics 14 (4), 046009. https://doi.org/10.1088/1748-3190/ab23e6.

Deng, J., Wang, S., Zhang, L., Mao, X., 2019b. Why does a flying fish taxi on sea surface before take-off? A hydrodynamic interpretation. bioRxiv, 765560. https://doi.org/10.1101/765560.

Fish, F., 1990. Wing design and scaling of flying fish with regard to flight performance. J. Zool. 221 (3), 391–403. https://doi.org/10.1111/j.1469-7998.1990.tb04009.x.

Gao, A., Techet, A.H., 2011. Design Considerations for a Robotic Flying Fish. OCEANS'11 MTS/IEEE KONA, pp. 1–8. https://doi.org/10.23919/OCEANS.2011.6107039.

Han, P., Lauder, G.V., Dong, H., 2020. Hydrodynamics of median-fin interactions in fish-like locomotion: effects of fin shape and movement. Phys. Fluids 32 (1), 011902. https://doi.org/10.1063/1.5129274.

Hedrick, T., 2008. Software techniques for two-and three-dimensional kinematic measurements of biological and biomimetic systems. Bioinspiration Biomimetics 3 (3), 034001. https://doi.org/10.1088/1748-3182/3/3/034001.

Hertel, H., 1966. Take-off and flight of the flying fish. Structure-Form-Movement 218–224.

Hubbs, C., 1933. Observations on the flight of fishes, with a statistical study of the flight of the Cypselurinae and remarks on the evolution of the flight of fishes. Pap. Mich. Acad. Sci. Arts Lett. 17, 575–611.

Khosronejad, A., Mendelson, L., Techet, A.H., Kang, S., Angelidis, D., Sotiropoulos, F., 2020. Water exit dynamics of jumping archer fish: integrating two-phase flow large-eddy simulation with experimental measurements. Phys. Fluids 32 (1), 011904. https://doi.org/10.1063/1.5130886.

Kumar, E.D., Sannasiraj, S.A., Sundar, V., Polnikov, V.G., 2013. Wind-wave characteristics and climate variability in the Indian Ocean region using altimeter data. Mar. Geodesy 36 (3), 303–318. https://doi.org/10.1080/01490419.2013.771718.

Latimer-Needham, C., 1951. Flying-fish aerodynamics. Flight 26, 535–536.

Liu, F., Lee, K.M., Yang, C.J., 2011. Hydrodynamics of an undulating fin for a wave-like locomotion system design. IEEE/ASME Trans. Mech. 17 (3), 554–562. https://doi.org/10.1109/TMECH.2011.2107747.

Lock, R.J., Burgess, S.C., Vaidyanathan, R., 2013. Multi-modal locomotion: from animal to application. Bioinspiration Biomimetics 9 (1), 011001. https://doi.org/10.1088/1748-3182/9/1/011001.

Mallock, A., 1928. Some modes of mechanical and animal locomotion. Nature 121, 541–545. https://doi.org/10.1038/121541a0.

Mccullough, G.B., Gault, D.E., 1951. Examples of Three Representative Types of Airfoil-Section Stall at Low Speed. NACA-TN-2502.

Mendelson, L., Techet, A.H., 2018. Multi-camera volumetric PIV for the study of jumping fish. Exp. Fluid 59 (1), 10. https://doi.org/10.1007/s00348-017-2468-x.

Moise, E.E., 1967. Calculus: Complete. Addison-Wesley, Reading.

Murray, M.P., Seireg, A., Scholz, R.C., 1967. Center of gravity, center of pressure, and supportive forces during human activities. J. Appl. Physiol. 23 (6), 831–838. https://doi.org/10.1152/jappl.1967.23.6.831.

Nelson, J.S., Grande, T.C., Wilson, M.V., 2016. Fishes of the World. John Wiley and Sons.

Nguyen, K., Au, L.T.K., Phan, H.V., Park, H.C., 2021a. Comparative dynamic flight stability of insect-inspired flapping-wing micro air vehicles in hover: longitudinal and lateral motions. Aero. Sci. Technol. 119, 107085 https://doi.org/10.1016/j.ast.2021.107085.

Nguyen, K., Au, L.T.K., Phan, S.H., Park, H.V., Park, H.C., 2021b. Effects of wing kinematics, corrugation, and clap-and-fling on aerodynamic efficiency of a hovering insect-inspired flapping-wing micro air vehicle. Aero. Sci. Technol. 118, 106990 https://doi.org/10.1016/j.ast.2021.106990.

Nguyen, K., Pham, T.H., Park, H.C., 2022a. Numerical estimation of hydrodynamic thrust using the measured tail-beating kinematics of a fish-like robot. In: The 18th International Conference on Intelligent Unmanned Systems (ICIUS). Tokoshima University, Tokushima, Japan.

Nguyen, K., Pham, T.H., Park, H.C., 2022b. Numerical investigation of hydrodynamics for a fish-like robot under undulatory forward swimming. In: Annual Meeting of Korean Society of Mechanical Engineering, ICC. Jeju, South Korea.

Ordaz, I., Geiselhart, K.A., Fenbert, J.W., 2015. Conceptual design of low-boom aircraft with flight trim requirement. J. Aircraft 52 (3), 932–939. https://doi.org/10.2514/1.C033160.

Park, H., Choi, H., 2010. Aerodynamic characteristics of flying fish in gliding flight. J. Exp. Biol. 213 (19), 3269–3279. https://doi.org/10.1242/jeb.046052.

Pham, T.H., Nguyen, K., Park, H.C., 2023. A robotic fish capable of fast underwater swimming and water leaping with high Froude number. Ocean Eng. 268, 113512 https://doi.org/10.1016/j.oceaneng.2022.113512.

Phan, H.V., Kang, T., Park, H.C., 2017. Design and stable flight of a 21 g insect-like tailless flapping wing micro air vehicle with angular rates feedback control. Bioinspiration Biomimetics 12 (3), 036006. https://doi.org/10.1088/1748-3190/aa65db.

Riddle, D.F., 1970. Calculus and Analytic Geometry, second ed. Wadsworth Publishing, Belmont, California, p. 566.

Salazar, R., Fuentes, V., Abdelkefi, A., 2018. Classification of biological and bioinspired aquatic systems: a review. Ocean Eng. 148, 75–114. https://doi.org/10.1016/j.oceaneng.2017.11.012.

Schlichting, H., 1979. Boundary-Layer Theory, seventh ed. U.S.A: McGraw Hill, New York.

Siddall, R., Kovač, M., 2014. Launching the AquaMAV: bioinspired design for aerial–aquatic robotic platforms. Bioinspiration Biomimetics 9 (3), 031001. https://doi.org/10.1088/1748-3182/9/3/031001.

Siddall, R., Ortega Ancel, A., Kovač, M., 2017. Wind and water tunnel testing of a morphing aquatic micro air vehicle. Interface Focus 7 (1), 20160085. https://doi.org/10.1098/rsfs.2016.0085.

Sihite, E., Kalantari, A., Nemovi, R., Ramezani, A., Gharib, M., 2023. Multi-Modal Mobility Morphobot (M4) with appendage repurposing for locomotion plasticity enhancement. Nat. Commun. 14 (1), 3323. https://doi.org/10.1038/s41467-023-39018-y.

Suzuki, H., Kato, N., 2005. A numerical study on unsteady flow around a mechanical pectoral fin. In: In the Fifteenth International Offshore and Polar Engineering Conference.

Tanaka, H., Li, G., Uchida, Y., Nakamura, M., Ikeda, T., Liu, H., 2019. Measurement of time-varying kinematics of a dolphin in burst accelerating swimming. PLoS One 14 (1), e0210860. https://doi.org/10.1371/journal.pone.0210860.

Truong, T.Q., Phan, H.V., Sane, S.P., Park, H.C., 2014. Pitching moment generation in an insect-mimicking flapping-wing system. J. Bionic. Eng. 11 (1), 36–51. https://doi.org/10.1016/S1672-6529(14)60018-4.

Withers, P., 1981. An aerodynamic analysis of bird wings as fixed aerofoils. J. Exp. Biol. 90 (1), 143–162. https://doi.org/10.1242/jeb.90.1.143.

Zeng, Z., Lyu, C., Bi, Y., Jin, Y., Lu, D., Lian, L., 2022. Review of hybrid aerial underwater vehicle: cross-domain mobility and transitions control. Ocean Eng. 248, 110840 https://doi.org/10.1016/j.oceaneng.2022.110840.

Zufferey, R., Ancel, A.O., Farinha, A., Siddall, R., Armanini, S.F., Nasr, M., Brahmal, R.V., Kennedy, G., Kovac, M., 2019. Consecutive aquatic jump-gliding with water-reactive fuel. Sci. Robot. 4 (34), eaax7330. https://doi.org/10.1126/scirobotics.aax7330.